Importance of cooling in triggering the collapse of hypermassive neutron stars

Vasileios Paschalidis, Zachariah B. Etienne, and Stuart L. Shapiro*

Department of Physics, University of Illinois at Urbana-Champaign, Urbana, Illinois 61801, USA

(Received 14 May 2012; published 18 September 2012)

The inspiral and merger of a binary neutron star (NSNS) can lead to the formation of a hypermassive neutron star (HMNS). As the HMNS loses thermal pressure due to neutrino cooling and/or centrifugal support due to gravitational wave emission, and/or magnetic breaking of differential rotation, it will collapse to a black hole. To assess the importance of shock-induced thermal pressure and cooling, we adopt an idealized equation of state and perform NSNS simulations in full general relativity through late inspiral, merger, and HMNS formation, accounting for cooling. We show that thermal pressure contributes significantly to the support of the HMNS against collapse and that thermal cooling accelerates its "delayed" collapse. Our simulations demonstrate explicitly that cooling can induce the catastrophic collapse of a *hot* hypermassive neutron star formed following the merger of binary neutron stars. Thus, cooling physics is important to include in NSNS merger calculations to accurately determine the lifetime of the HMNS remnant and to extract information about the neutron star equation of state, cooling mechanisms, bar instabilities and B-fields from the gravitational waves emitted during the transient phase prior to black hole formation.

DOI: 10.1103/PhysRevD.86.064032 PACS numbers: 04.25.D−, 04.25.dk, 04.30.−w

I. INTRODUCTION

The inspiral and merger of compact binaries has attracted considerable attention in recent years for two main reasons. First, such systems emit a large flux of gravitational waves (GWs), making them among the most promising sources for GWs detectable by ground-based laser interferometers, such as LIGO [1,2], VIRGO [3,4], GEO [5], and KAGRA [6], as well as by proposed space-based interferometers, such as eLISA/NGO [7] and DECIGO [8]. Second, black hole-neutron star (BHNS) and neutron star-neutron star (NSNS) mergers are candidates for the central engines that power the observed short-hard gamma ray bursts (sGRBs).

Extracting physical information about these binaries from their GWs and their accompanying electromagnetic signals may reveal critical details about the equation of state of neutron star matter and may unveil the nature of the sGRB phenomenon. However, interpreting the data requires careful modeling of these systems in full general relativity (see Ref. [9] for a comprehensive review and references). Most effort in general relativity to date has focused on modeling black hole-black hole (BHBH) binaries (see also Ref. [10]), and NSNS binaries (see also Ref. [11]), with some recent work on BHNS binaries (see also Ref. [12]), and white dwarf-neutron star binaries [13–15].

NSNSs are known to exist, which makes NSNS systems particularly attractive to study. Theoretical calculations show that NSNS mergers can lead to the formation of a hypermassive neutron star. A HMNS [16] is a differentially rotating neutron star (NS) whose mass exceeds the maximum mass of a uniformly rotating star [17,18]. The latter is about 20% larger than the maximum mass of a nonrotating (spherical) equilibrium star [the Tolman-Oppenheimer-Volkoff (TOV) limit] [16]. Typically a HMNS forms following the merger of a NSNS, when the system's total mass is smaller than some threshold mass $M_{\rm th}$. According to Ref. [19] this threshold mass is $M_{\rm th} \approx 1.3$–$1.35 M_{\rm sph}$, where $M_{\rm sph}$ is the TOV limit for the same equation of state (EOS).

A HMNS is a transient, quasiequilibrium configuration. It will eventually undergo "delayed collapse" on a secular (dissipative) time scale, which may power a sGRB. There are two distinct routes by which this collapse might be triggered:

(1) If the HMNS is primarily centrifugally supported, redistribution of angular momentum by viscosity or magnetic fields [20,21], and/or loss of angular momentum by GW emission [22] destroys the support provided, leading to catastrophic collapse.
(2) If the HMNS is primarily supported by thermal pressure generated by shocks during merger, delayed collapse may be triggered by the loss via neutrino cooling of thermal energy [23].

While catastrophic collapse of a *cold* HMNS via viscosity or magnetic fields has been demonstrated using fully general relativistic calculations [20,21], there are no fully general relativistic calculations to date that demonstrate explicitly that cooling can induce collapse of a hot HMNS produced following the merger of binary neutron stars.

HMNSs formed in NSNS mergers will always be hot due to shock heating. *A priori* it is not clear which mechanism is most important for holding up a HMNS against collapse: centrifugal forces or thermal pressure. The answer to this question is still open and may depend on the nature of the companions (e.g., masses, EOS etc.).

*Also at Department of Astronomy and NCSA, University of Illinois at Urbana-Champaign, Urbana, IL 61801, USA.

 © 2012 American Physical Society

Recent simulations of binary NS mergers that form hypermassive NSs seem to point in different directions. For example, in Refs. [25,26] an equal-mass NSNS is evolved assuming a $\Gamma = 2$ EOS. It is shown that angular momentum carried away by gravitational waves alone can induce the collapse. Reference [27] also evolves an equal-mass NSNS, but with a more realistic, finite temperature, nuclear EOS. They find that the deviation of their HMNSs from axisymmetry is so small that GW emission is significantly reduced. The authors argue that shock heating is sufficiently important that their HMNSs are supported by the excess thermal pressure.

Determining which mechanism controls the lifetime of the remnant is important because it determines the time interval between the NSNS merger and the delayed collapse—a time interval that can in principle be measured by Advanced LIGO/VIRGO. It is the time interval between the end of the gravitational wave signal due to the inspiral and the beginning of the burst signal due to the delayed collapse. If differential rotation support is most important, then the time interval is governed by, e.g., the Alfvén time scale, assuming magnetic braking of differential rotation is most important, or the GW time scale, in the case of a rapidly spinning remnant that develops a bar. By contrast, if thermal pressure is dominant, then the time scale is governed by thermal cooling. Therefore, knowing the mechanism driving collapse may place constraints on seed magnetic field magnitudes, or the existence of bar modes, or the relevant cooling mechanisms. It could even place constraints on the temperature of matter, as well as the nuclear EOS.

To disentangle the effects of thermal support from those of rotational support, previous studies compared results from NSNS simulations that suppress shocks (by enforcing a strictly cold EOS) to those that allow shocks. If the HMNS remnant lives longer with shocks than without, then it is tempting to infer that thermal pressure due to shock heating is chiefly responsible for supporting the remnant. However, it is not possible to draw such a firm conclusion because shocks, which act on a hydrodynamical time scale, not only heat the gas, thereby increasing the total pressure support, but also affect the matter and angular momentum profiles. Different profiles can themselves increase the lifetime of a HMNS.

The goal of this paper is to study the relative importance of thermal pressure in supporting HMNSs from collapse and demonstrate that cooling can induce the catastrophic collapse of a HMNS formed following the merger of binary neutron stars. We accomplish this by performing a limited set of NSNS simulations in full GR through late inspiral, merger, (hot) HMNS formation, and collapse. We account for cooling in the HMNS remnant via a covariant cooling scheme we developed in Ref. [14]. We then compare this HMNS evolution to a control simulation, in which the cooling mechanism is disabled.

Our simulations model the initial NSNS binary as equal-mass, irrotational, quasiequilibrium $n = 1$ polytropes in a quasicircular orbit, corresponding to case 1.46–45–$*$ of Ref. [25].

Following the NSNS merger, a quasiequilibrium HMNS forms. We then continue the evolution of the remnant with and without cooling, which we model via an effective local emissivity. For the runs with cooling, we choose two cooling time scales. We find that, independent of the cooling time scale chosen, the HMNS collapses and forms a black hole (BH) within a few cooling time scales.

Our simulations suggest that shock-induced thermal pressure is a significant source of support against gravitational collapse, even in the case of polytropic NSs and demonstrate explicitly that cooling can induce the catastrophic collapse of a HMNS. Estimating the temperature of the remnant, we find that a realistic neutrino cooling time scale is of order a few 100 ms. Given that our estimated cooling time scale is comparable to the angular momentum redistribution/loss time scales due to either magnetic braking or GWs, our results suggest that accounting for cooling is a critical ingredient in predicting the lifetime of a HMNS. Accordingly, cooling physics must be incorporated in models of binary NS simulations.

The paper is structured as follows. In Sec. II we review the time scales relevant to HMNSs formed in binary NSNS mergers. Sections III and IV summarize the initial data, basic evolution equations, numerical methods, and cooling formalism. The basic results are presented in Sec. V and summarized in Sec. VI. Throughout this work, geometrized units are adopted, where $G = c = 1$, unless otherwise specified.

II. TIME SCALES

The relevant time scales in the evolution of a typical HMNS formed in NSNS mergers are its rotation period T, the gravitational wave time scale $t_{\rm GW}$, the cooling time scale $t_{\rm cool}$, and Alfvén time scale $t_{\rm A}$. We provide rough estimates of these time scales in this section.

A. Rotation period

We express the HMNS angular frequency Ω as some fraction ϵ of the break-up angular frequency $\Omega_{\rm ms}$

$$\Omega \approx \epsilon\sqrt{\frac{M}{R^3}}, \tag{1}$$

where M is the HMNS mass and R its radius. The rotation period of the HMNS can then be written as

$$T \equiv \frac{2\pi}{\Omega} = \frac{2\pi R^{3/2}}{\epsilon M^{1/2}} \approx 2\left(\frac{\epsilon}{0.5}\right)^{-1}\left(\frac{R}{20\ \text{km}}\right)^{3/2}\left(\frac{M}{2.8M_\odot}\right)^{-1/2}\ \text{ms}. \tag{2}$$

For the numerical estimate we have used the values for the mass and radius of a typical HMNS remnant.

B. Gravitational wave time scale

GW emission sets the time scale of angular momentum loss from the system. The gravitational wave time scale for a triaxial, incompressible, spinning ellipsoid with ellipticity e can be estimated as [28]

$$t_{\rm GW} \equiv \frac{J}{dJ/dt} \approx \frac{1}{MR^2\Omega^4 e^2} = \frac{R^4}{\epsilon^4 e^2 M^3} \approx 200\left(\frac{\epsilon}{0.5}\right)^{-4}\left(\frac{e}{0.75}\right)^{-2}\left(\frac{R}{20\ \rm km}\right)^{4}\left(\frac{M}{2.8M_\odot}\right)^{-3}\ \rm ms, \quad (3)$$

where $J \approx MR^2\Omega$ is the HMNS angular momentum and the ellipticity is defined as

$$e = \frac{a-b}{R}, \quad (4)$$

where a is the semimajor axis of the HMNS, b the semiminor axis, and R is $(a+b)/2$. To estimate the time scale, we assumed a value for the ellipticity that corresponds to a plausible bar. Note also that our estimated $t_{\rm GW}$ is comparable to the GW time scale inferred by direct numerical simulations in Ref. [26].

C. Cooling Time Scale

HMNSs are cooled predominantly by emission of neutrinos. At densities $\gtrsim 10^{11}$ g/cm^3 neutrinos become trapped [28]. Therefore, the cooling time scale is set by the time it takes for the neutrinos to diffuse out of the hot HMNS remnant. The main sources of opacity are free nucleon scattering and neutrino absorption by nucleons (since protons and neutrons comprise the bulk of the HMNS). The diffusion time scale can be estimated as [29]

$$t_{\rm cool} \approx 3\frac{R^2}{\lambda_n c}, \quad (5)$$

where λ_n is the mean free path of the neutrinos given by

$$\lambda_n^{-1} = n\sigma_n, \quad (6)$$

where n is the neutron number density [30], σ_n is the total interaction cross section $\sigma_n = \sigma_{\rm scat} + \sigma_{\rm abs}$, where the elastic scattering and absorption cross sections are respectively given by [28,29]

$$\sigma_{\rm scat} \approx \frac{1}{4}\sigma_0\left(\frac{E_\nu}{m_e c^2}\right)^2, \qquad \sigma_{\rm abs} \approx 1.42\sigma_0\left(\frac{E_\nu}{m_e c^2}\right)^2, \quad (7)$$

where $\sigma_0 = 1.76\times 10^{-44}$ cm^2, m_e is the electron mass, and E_ν the neutrino energy. Substituting Eqs. (6) and (7) in Eq. (5) we find

$$t_{\rm cool} \approx \frac{15M\sigma_0(E_\nu/m_e c^2)^2}{4\pi m_{\rm n} Rc} \approx 400\left(\frac{M}{2.8M_\odot}\right)\left(\frac{R}{20\ \rm km}\right)^{-1}\left(\frac{E_\nu}{10\ \rm MeV}\right)^2\ \rm ms, \quad (8)$$

where $n = \bar{\rho}/m_n$, with $\bar{\rho} = 3M/4\pi R^3$ the mean HMNS density, and m_n the mass of a neutron. For the numerical estimates above we used typical rms values for the neutrino energy of order 10 MeV, as found in the simulations of Ref. [29]. Note that for typical neutrino energies of 20 MeV found in Ref. [27], the neutrino cooling timescale is $\sim$2 s. Both of these works used approximate neutrino transfer schemes. We see that obtaining a neutrino cooling time scale depends on identifying the energy(ies) of typical neutrino(s), which in turn requires accurate modeling of not only bulk motion but also the microphysics.

D. Alfvén time scale

Magnetic fields set the time scale for the braking of differential rotation in typical HMNSs. This occurs on the Alfvén time scale [21], given by

$$t_{\rm A} \approx \frac{R}{v_A} \approx \frac{R\sqrt{4\pi\rho}}{B} \approx 100\left(\frac{R}{20\ \rm km}\right)^{-1/2}\left(\frac{M}{2.8M_\odot}\right)^{1/2}\left(\frac{B}{10^{15}\ \rm G}\right)^{-1}\ \rm ms, \quad (9)$$

where v_A is the Alfvén velocity, and where a strong but dynamically unimportant interior magnetic field has been assumed for the numerical estimate. While little is known about the strength of NS *interior* magnetic fields, the value appearing in (9) is consistent with magnetars models [31]. In addition, NSNS simulations indicate that magnetic instabilities can amplify interior B-fields from $\sim 10^{12}$ G to $\sim 10^{15}$ G during merger [32].

E. Time scale summary

These time scale estimates indicate that the neutrino cooling time scale can be comparable to the magnetic braking/angular momentum loss time scales in typical HMNSs. If thermal pressure is the dominant source of support in an HMNS against catastrophic collapse to a BH, then the cooling time scale will determine the time interval between the GW signals at merger and collapse. Even if thermal pressure contributes only partially to the support of the HMNS, the remnant will collapse faster with cooling than without. These considerations necessitate the modeling of neutrino cooling in simulations of NSNS mergers that form HMNSs, not only to predict the neutrino signature but also to determine what mechanism drives the remnant to its final configuration. Knowing the results from such simulations, it may be possible to extract useful information about the temperature of the matter, neutrino cooling mechanisms, the existence of bar modes, and the magnetic field strength and possibly place constraints on

the nuclear EOS from the GW observations. We perform preliminary simulations to probe this issue below.

III. BASIC EQUATIONS

This section introduces our notation, summarizes our methods and numerical techniques as described in Refs. [33–36]. Greek indices denote all four spacetime dimensions (0, 1, 2, and 3), and Latin indices label spatial parts only (1, 2, and 3).

We use the 3 + 1 formulation of general relativity and decompose the metric into the following form:

$$ds^2 = -\alpha^2 dt^2 + \gamma_{ij}(dx^i + \beta^i dt)(dx^j + \beta^j dt). \quad (10)$$

The fundamental variables for metric evolution are the spatial three-metric γ_{ij} and extrinsic curvature K_{ij}. We adopt the Baumgarte-Shapiro-Shibata-Nakamura (BSSN) formalism [37,38] in which the evolution variables are the conformal exponent $\phi \equiv \ln(\gamma)/12$, the conformal 3-metric $\tilde{\gamma}_{ij} = e^{-4\phi}\gamma_{ij}$, three auxiliary functions $\tilde{\Gamma}^i \equiv -\tilde{\gamma}^{ij}{}_{,j}$, the trace of the extrinsic curvature K, and the trace-free part of the conformal extrinsic curvature $\tilde{A}_{ij} \equiv e^{-4\phi}(K_{ij} - \gamma_{ij}K/3)$. Here, $\gamma = \det(\gamma_{ij})$. The full spacetime metric $g_{\mu\nu}$ is related to the three-metric $\gamma_{\mu\nu}$ by $\gamma_{\mu\nu} = g_{\mu\nu} + n_\mu n_\nu$, where the future-directed, timelike unit vector n^μ normal to the time slice can be written in terms of the lapse α and shift β^i as $n^\mu = \alpha^{-1}(1, -\beta^i)$. Evolution equations for these BSSN variables are given by Eqs. (9)–(13) in Ref. [33]. We adopt the standard puncture gauge conditions: an advective "1 + log" slicing condition for the lapse and a "Γ-freezing" condition for the shift [39]. The evolution equations for α and β^i are given by Eqs. (2)–(4) in Ref. [34], with the η parameter set to $0.2/M$, where M is the Arnowitt-Deser-Misner (ADM) mass of the NSNS binary. We add a fifth-order Kreiss-Oliger dissipation term to all evolved BSSN, lapse and shift variables to reduce high-frequency numerical noise associated with adaptive-mesh-refinement (AMR) interfaces.

The fundamental hydrodynamic variables are the rest-mass density ρ_0, specific internal energy ϵ, pressure P, and four-velocity u^μ. We adopt a Γ-law EOS $P = (\Gamma - 1)\rho_0\epsilon$ with $\Gamma = 2$, which reduces to an $n = 1$ polytropic law $[P = \kappa\rho_0^{(1+1/n)}]$ for the initial (cold) neutron star matter. The fluid stress-energy tensor is given by

$$T_{\mu\nu} = \rho_0 h u_\mu u_\nu + P g_{\mu\nu}, \quad (11)$$

where $h = 1 + \epsilon + P/\rho_0$ is the specific enthalpy.

In the standard numerical implementation of the general relativistic hydrodynamic (GRHD) equations using a conservative scheme, it is useful to introduce the "conservative" variables ρ_*, $\tilde{S}_i$, $\tilde{\tau}$. They are defined as

$$\rho_* \equiv -\sqrt{\gamma}\rho_0 n_\mu u^\mu, \quad (12)$$

$$\tilde{S}_i \equiv -\sqrt{\gamma}T_{\mu\nu}n^\mu\gamma_i^\nu, \quad (13)$$

$$\tilde{\tau} \equiv \sqrt{\gamma}T_{\mu\nu}n^\mu n^\nu - \rho_*. \quad (14)$$

The evolution equations for ρ_*, $\tilde{S}_i$ and $\tilde{\tau}$ can be derived from the conservation of rest mass $\nabla_\mu(\rho_* u^\mu) = 0$ and the conservation of energy-momentum $\nabla_\mu T^{\mu\nu} = 0$, giving rise to Eqs. (27)–(30) in Ref. [35].

IV. NUMERICAL METHODS

A. Initial data

For initial data we choose an irrotational NSNS system in a quasiequilibrium circular orbit that consists of equal-mass, $n = 1$ polytropic NSs. The initial data satisfy the conformal thin sandwich equations [9], have been calculated using the LORENE spectral methods numerical libraries [40] and are publicly available. These data apply to a configuration with arbitrary κ, compaction (in isolation) $M/R = 0.12$, where the compaction of the maximum mass configuration is $M/R = 0.216$. Each star has a rest mass that is 72% of the maximum allowable TOV rest mass for this EOS. The initial cold configuration has a coordinate separation of $11.31M$, where M is the ADM mass of system, with $M\Omega = 0.024$, where Ω is the angular frequency of the system. The ADM angular momentum of the system is $J/M^2 = 1.02$. We note here that our initial data correspond to case 1.46–45–∗ of Ref. [25] and that they can be considered as the polytropic counterpart of case H studied in Ref. [27]. If we set $\kappa = 393.9$ km^2, the ADM mass of our stars in isolation becomes $1.59M_\odot$, which is very close to the ADM mass ($1.6M_\odot$) in isolation of case H in Ref. [27], where a finite temperature EOS was adopted that yields for zero-temperature matter a maximum TOV mass of $2.2M_\odot$.

B. Evolution of the metric and matter

We evolve the BSSN equations with fourth-order accurate, centered finite-differencing stencils, except on shift advection terms, where we use fourth-order accurate upwind stencils. We apply Sommerfeld outgoing wave boundary conditions to all BSSN fields. Our code is embedded in the CACTUS parallelization framework [41], and our fourth-order Runge-Kutta time stepping is managed by the MOL (Method of Lines) thorn, with a Courant-Friedrichs-Lewy factor set to 0.45. We use the CARPET [42] infrastructure to implement the moving-box adaptive mesh refinement. In all AMR simulations presented here, we use second-order temporal prolongation, coupled with fifth-order spatial prolongation.

The GRHD equations are evolved via a high-resolution shock-capturing technique [43] that employs piecewise parabolic method (PPM) [44] coupled to the Harten, Lax, and van Leer approximate Riemann solver [45]. The adopted GRHD scheme is second-order accurate for smooth flows, and first-order accurate when discontinuities (e.g., shocks) arise. To stabilize our scheme in regions

where there is no matter, we maintain a tenuous atmosphere on our grid, with a density floor $\rho_{\rm atm}$ set equal to 10^{-10} times the initial maximum density on our grid. The initial atmospheric pressure $P_{\rm atm}$ is set equal to the cold polytropic value $P_{\rm atm} = \kappa\rho_{\rm atm}^{\Gamma}$. Throughout the evolution, we impose limits on the atmospheric pressure to prevent spurious heating and negative values of the internal energy ϵ due to numerical errors. Specifically, we require $P_{\rm min} \le P \le P_{\rm max}$, where $P_{\rm max} = 10\kappa\rho_0^{\Gamma}$ and $P_{\rm min} = \kappa\rho_0^{\Gamma}/2$. Whenever P exceeds $P_{\rm max}$ or drops below $P_{\rm min}$, we reset P to $P_{\rm max}$ or $P_{\rm min}$, respectively. We impose these pressure limits only in regions where the rest-mass density remains very low ($\rho_0 < 100\rho_{\rm atm}$), as in Ref. [34].

C. Radiative cooling

We now briefly describe our method for implementing cooling in our simulations. For a derivation and details regarding this covariant cooling method, see Ref. [14].

The dynamics of radiation is governed by [46–48]

$$\nabla_\alpha R^{\alpha\beta} = -G^\beta, \tag{15}$$

where $R^{\alpha\beta}$ is the radiation stress-energy tensor given by

$$R^{\alpha\beta} = \int d\nu d\Omega I_\nu N^\alpha N^\beta, \tag{16}$$

and G^α is the radiation four-force density given by

$$G^\alpha = \int d\nu d\Omega(\chi_\nu I_\nu - j_\nu)N^\alpha. \tag{17}$$

In the equations above, $d\Omega$ is the solid angle, ν and $I_\nu = I_\nu(x^\alpha, N^i, \nu)$ are the radiation frequency and specific intensity of radiation at x^α moving in direction $N^\alpha = p^\alpha/h\nu$, respectively. All quantities are measured in the local Lorentz frame of a fiducial observer with four-velocity $u^\alpha_{\rm fid}$, i.e.,

$$h\nu = -p_\alpha u^\alpha_{\rm fid}, \tag{18}$$

where p^α is the photon four-momentum and h denotes Planck's constant. The energy-momentum conservation equation then becomes

$$\nabla_\alpha(T^{\alpha\beta} + R^{\alpha\beta}) = 0 \tag{19}$$

or after using Eq. (15),

$$\nabla_\alpha T^{\alpha\beta} = G^\beta. \tag{20}$$

Our artificial cooling prescription amounts to finding a functional form for G^β such that thermal energy and pressure are drained from the system. Choosing

$$G^\alpha = -u^\alpha\Lambda, \tag{21}$$

and setting

$$\Lambda = \frac{\rho_0}{\tau_c}\epsilon_{\rm th}, \tag{22}$$

where τ_c is some prescribed cooling time scale, it can be shown that in a frame comoving with the fluid, the specific thermal energy of a fluid parcel evolves as follows [14]

$$\frac{d}{d\tau}\epsilon_{\rm th} = \left[\frac{(\Gamma_{\rm th}-1)}{\rho_0}\frac{d\rho_0}{d\tau} - \frac{1}{\tau_c}\right]\epsilon_{\rm th}, \tag{23}$$

where τ is the proper time of a comoving observer.

The first term in brackets on the rhs of Eq. (23) arises from adiabatic compression or expansion. The second term corresponds to cooling and radiates away thermal energy exponentially.

Projecting Eq. (20) using the timelike unit vector n^α normal to spacelike hypersurfaces and the projection operator $h^\alpha{}_\beta = \delta^\alpha{}_\beta + n^\alpha n_\beta$, we find that the 3 + 1 GRHD equations become

$$\partial_t\tilde{S}_i + \partial_j(\alpha\sqrt{\gamma}T^j{}_i) = \frac{1}{2}\alpha\sqrt{\gamma}T^{\alpha\beta}g_{\alpha\beta,i} - \alpha\sqrt{\gamma}u_i\Lambda, \tag{24}$$

and

$$\partial_t\tilde{\tau} + \partial_i(\alpha^2\sqrt{\gamma}T^{0i} - \rho_* v^i) = s - \alpha^2\sqrt{\gamma}u^0\Lambda, \tag{25}$$

where we have used Eq. (21). Thus cooling enters as a source term in the GRHD equations.

D. Recovery of primitive variables

At each time step, we need to recover the "primitive variables" ρ_0, P, and v^i from the "conservative" variables ρ_*, $\tilde{\tau}$, and $\tilde{S}_i$. We perform the inversion by numerically solving two nonlinear equations via the Newton-Raphson method as described in Ref. [49], using the code developed in Ref. [50].

Sometimes the "conservative" variables may assume values which are out of physical range, resulting in unphysical primitive variables after inversion (e.g., negative pressure or even complex solutions). This usually happens in the low-density "atmosphere" or deep inside the BH interior (when a BH is present) where high-accuracy evolution is difficult to maintain. Various techniques have been suggested to handle the inversion failure (see, e.g., Ref. [51]). Our approach is mainly to impose constraints on the conservative variables to reduce the inversion failure. For a summary of our latest techniques, see Ref. [52].

E. Diagnostics

1. Constraints and rest-mass conservation

During the evolution, we monitor the Hamiltonian and momentum constraints, calculated by Eqs. (40)–(43) of Ref. [33].

When hydrodynamic matter is evolved on a fixed uniform grid, our hydrodynamic scheme guarantees that the rest mass M_0 is conserved to machine roundoff error. This strict conservation is no longer maintained in an AMR grid, where spatial and temporal prolongation is performed at

the refinement boundaries. Hence, we also monitor the total rest mass,

$$M_0 = \int \rho_* d^3x, \tag{26}$$

during the evolution. Rest-mass conservation is also violated whenever ρ_0 spuriously drops below and is then reset to the atmosphere value. This usually happens only in the very low-density atmosphere or deep inside the BH horizon where high accuracy is difficult to maintain. In the simulations presented in this paper the violation of rest-mass conservation is less than 1%.

2. Temperature

We measure the thermal energy generated by shocks via the entropy parameter $K \equiv P/P_{\rm cold}$, where $P_{\rm cold} = \kappa\rho_0^\Gamma$ is the pressure associated with the cold EOS. The specific internal energy can be decomposed into a cold part and a thermal part: $\epsilon = \epsilon_{\rm cold} + \epsilon_{\rm th}$ with

$$\epsilon_{\rm cold} = -\int P_{\rm cold} d(1/\rho_0) = \frac{\kappa}{\Gamma - 1}\rho_0^{\Gamma-1}. \tag{27}$$

Hence, the relationship between K and $\epsilon_{\rm th}$ is

$$\begin{aligned}\epsilon_{\rm th} &= \epsilon - \epsilon_{\rm cold} = \frac{1}{\Gamma-1}\frac{P}{\rho_0} - \frac{\kappa}{\Gamma-1}\rho_0^{\Gamma-1} \\ &= (K-1)\epsilon_{\rm cold}.\end{aligned} \tag{28}$$

For shock-heated gas, we always have $K > 1$ (see Appendix B of Ref. [34].

To estimate the temperature of the remnant we model the specific thermal energy as

$$\epsilon_{\rm th} = \frac{3k{\rm T}}{2m_{\rm n}} + f\frac{a{\rm T}^4}{\rho_0}, \tag{29}$$

where $m_{\rm n}$ is the mass of a nucleon, k is Boltzmann's constant and a is the radiation constant. The first term represents the approximate thermal energy of the nucleons, and the second term accounts for the thermal energy due to relativistic particles. The factor f reflects the number of species of relativistic particles that contribute to the thermal energy and is determined self-consistently as outlined in Ref. [14].

Note that the value of T depends on the adopted mass of the initial configuration and breaks the scale invariance with respect to κ. For this purpose we set $\kappa = 269.6$ km^2, for which $M = 2.69M_\odot$.

3. GW extraction, energy and angular momentum conservation

Gravitational waves are extracted using the Newman-Penrose Weyl scalar ψ_4 at various extraction radii between 40 and $150M$. We decompose ψ_4 into $s = -2$ spin-weighted spherical harmonics up to and including $l = 4$ modes. At each extraction radius, the retarded time is computed using the technique described in Sec. IIB of Ref. [53] to reduce the near-field effect.

We compute the radiated energy ΔE_{GW} and z-component of angular momentum ΔJ_{GW} using expressions equivalent to Eqs. (33), (39), (40) and (49) of Ref. [54].

We also monitor the mass $M_{\rm int}$ and (z component of) the total angular momentum $J_{\rm int}$ interior to the simulation domain. These quantities are defined as integrals over the surface of the outer boundary ∂V) of the computational domain:

$$M_{\rm int} = \frac{1}{2\pi}\oint_{\partial V}\left(\frac{1}{8}\tilde{\Gamma}^i - \tilde{\gamma}^{ij}\partial_j\psi\right)d\Sigma_i, \tag{30}$$

$$J_{\rm int} = \frac{1}{8\pi}\tilde{\epsilon}^k_{zj}\oint_{\partial V} x^j(K^m_k - \delta^m_k K)d\Sigma_m, \tag{31}$$

where $\tilde{\epsilon}_{ijk}$ is the flat-space Levi-Civita tensor. As pointed out in Ref. [34], the integrals can be evaluated more accurately by alternative expressions that use Gauss's law [9]:

$$\begin{aligned}M_{\rm int} = &\int_V d^3x\left(\psi^5\rho + \frac{1}{16\pi}\psi^5\tilde{A}_{ij}\tilde{A}^{ij}\right. \\ &\left. - \frac{1}{16\pi}\tilde{\Gamma}^{ijk}\tilde{\Gamma}_{jik} + \frac{1-\psi}{16\pi}\tilde{R} - \frac{1}{24\pi}\psi^5K^2\right) \\ &+ \frac{1}{2\pi}\oint_S\left(\frac{1}{8}\tilde{\Gamma}^i - \tilde{\gamma}^{ij}\partial_j\psi\right)d\Sigma_i,\end{aligned} \tag{32}$$

$$\begin{aligned}J_{\rm int} = &\frac{1}{8\pi}\tilde{\epsilon}_{zj}{}^n\int_V d^3x\psi^6\left(\tilde{A}^j{}_n + \frac{2}{3}x^j\partial_n K - \frac{1}{2}x^j\tilde{A}_{km}\partial_n\tilde{\gamma}^{km}\right. \\ &\left. + 8\pi x^j\tilde{S}_n\right) + \frac{1}{8\pi}\tilde{\epsilon}_{zj}{}^n\oint_S\psi^6x^j\tilde{A}^m{}_n d\Sigma_m,\end{aligned} \tag{33}$$

where S is a surface surrounding the BH horizon (when a BH is present), V is the volume between S and the outer boundary, $\rho = n_\mu n_\nu T^{\mu\nu}$, and $\tilde{R}$ is the Ricci scalar associated with the conformal 3-metric $\tilde{\gamma}_{ij}$.

To check the violation of energy and angular momentum conservation, we monitor the quantities

$$\delta E = |M - M_{\rm int}(t) - \Delta E_{\rm GW}(t)|/M, \tag{34}$$

$$\delta J = |J - J_{\rm int}(t) - \Delta J_{\rm GW}(t)|/J, \tag{35}$$

where J and M are the ADM angular momentum and mass of the binary, respectively, and $M_{\rm int}(t)$ and $J_{\rm int}(t)$ are the total mass and angular momentum of the system at time t as calculated by Eqs. (32) and (33). Note that $J_{\rm int}(0) = J$, $M_{\rm int}(0) = M$, and $\delta E(0) = \delta J(0) = 0$ at $t = 0$. The maximum violation of energy conservation in the simulations we present in this paper is $\delta E = 2\%$ and the maximum angular momentum violation is $\delta J = 3.4\%$.

V. RESULTS

This section presents the results from our fully relativistic binary NS simulations with cooling. Following the

TABLE I. Summary of cases. The second column indicates whether cooling is applied. Here $M = 1.32 \times 10^{-5}(M_0/1.45M_\odot)$ s $= 3.98(M_0/1.45M_\odot)$ km is the ADM mass.

Case Name[a]	Cooling On	Cooling time scale, τ/M
A	No	∞
B1	Yes	150.82
B2	Yes	301.64

[a]The inspiral and merger calculation is part of case A. In cases B1 and B2 cooling is turned on at $t \approx 1600M$, at which point the HMNS remnant of case A has relaxed to a quasiequilibrium state.

merger and formation of a HMNS remnant, which were carried out without cooling, we perform three subsequent calculations. In one calculation cooling is never turned on (case A). In the other two calculations, cooling is triggered at $t \approx 1600M$, at which point the HMNS remnant has relaxed to a quasiequilibrium state—the rest-mass density has settled and is changing on a secular (GW) time scale. We continue the simulations with cooling, choosing either a short or a long cooling time scale, corresponding to case B1 and B2, respectively. Table I summarizes these different cases.

In addition, we performed all simulations at both moderate and high resolutions. The grid configurations are outlined in Table II. The results we obtained are insensitive to resolution, and for this reason all plots that follow correspond to data from our high-resolution runs.

A. Inspiral and merger

During inspiral and merger in case A, no cooling takes place. The evolution of the rest-mass density contours in the orbital plane are shown in Fig. 1. As gravitational waves carry angular momentum away from the system, the orbits become tighter, and the stars become strongly tidally distorted (top row, middle panel of Fig. 1). Shortly after the second orbit the stars collide (top row, right panel of Fig. 1), marking the onset of the merger phase. Half an orbit later, the shock-heated stars become strongly sheared (bottom row, left panel of Fig. 1) and eventually merge and settle in a quasiequilibrium configuration that consists of two cold cores, separated by hot, dense material and surrounded by a hot, dense mantle (bottom row, middle and right panels of Fig. 1). The upper panel of Fig. 2 shows the meridional rest-mass density contours at the same time as the final panel of Fig. 1. No mass outflows from the system are observed, so the HMNS has a rest mass approximately equal to the initial rest mass of the system. This mass now exists within an equatorial radius of about 20 km and a polar radius of about 12 km.

Figure 3 shows the evolution of the orbital-plane $K = P/P_{\rm cold}$ contours for case A at merger and following HMNS formation. The left panel in Fig. 3 shows how the collision of the two stars begins to shock heat the matter. In the middle and right panels in Fig. 3 the total pressure in the HMNS is clearly greater than the cold pressure everywhere except inside the two cores. Notice the existence of a hot area between the two cores of the remnant. In this area $K \approx 1.5$, indicating that the thermal pressure adds a total of 50% additional support to the cold pressure. In the outer layers of the remnant the thermal pressure provides up to $\sim$80% of the total pressure. The lower panel of Fig. 2 shows the meridional K contours. Notice that K approaches 1.8 in both the outer HMNS layers and the hot region between the double core. These results demonstrate that shock heating has enhanced the total pressure, which, along with centrifugal forces, contributes to the support of the remnant against gravitational collapse.

Following HMNS formation at about $t \approx 500M = 6.6(M/2.69M_\odot)$ ms, the remnant survives for a long quasistationary epoch, during which the maximum density increases almost linearly with time (see left panel of Fig. 4). Similar behavior is reported in Ref. [25] when using the same Γ-law EOS adopted here and no cooling.

In addition, Ref. [25] performed a simulation of the same system, but with a strict *polytropic* EOS ($P = \kappa\rho_0^\Gamma$), in which shocks are artificially suppressed. In this case, it is found that the resulting HMNS collapsed when $\rho_{0,\rm max} \approx 2\rho_{0,\rm max,initial}$ at which point $t \approx 21$ ms. Applying this same density criterion to the Γ-law EOS, they extrapolate that the HMNS would collapse at $t \approx 110(M/2.69M_\odot)$ ms. Our simulations show that $\rho_{0,\rm max} \approx 2\rho_{0,\rm max,initial}$ at $t \approx 105(M/2.69M_\odot)$ ms, in good agreement with Ref. [25]'s result. In a follow-up calculation [26], the same authors demonstrate that the HMNS remnant collapses to a BH at $t \approx 130(M/2.69M_\odot)$ ms.

In the polytropic EOS simulation (shocks disallowed), centrifugal forces provide the only source of support against collapse and $t_{\rm coll} \sim t_{\rm GW}$. However, in the Γ-law

TABLE II. Grid configurations. Here, $N_{\rm NS}$ denotes the number of grid points covering the smallest diameter of the neutron star initially (13.54 km $= 3.4M$). "Moderate" indicates the moderate resolution runs, and "High" the high resolution ones.

Grid Hierarchy (in units of M)[a]		Max. resolution	$N_{\rm NS}$
Moderate	(181.98, 90.488, 45.244, 22.622, 15.081, 11.311, 7.541, 5.302)	$M/16.97$	116
High	(181.98, 90.488, 45.244, 22.622, 15.081, 11.311, 7.541, 5.043)	$M/21.22$	144

[a]There are two sets of nested refinement boxes centered on each of the NSs. This column specifies the half side length of the refinement boxes centered on each star.

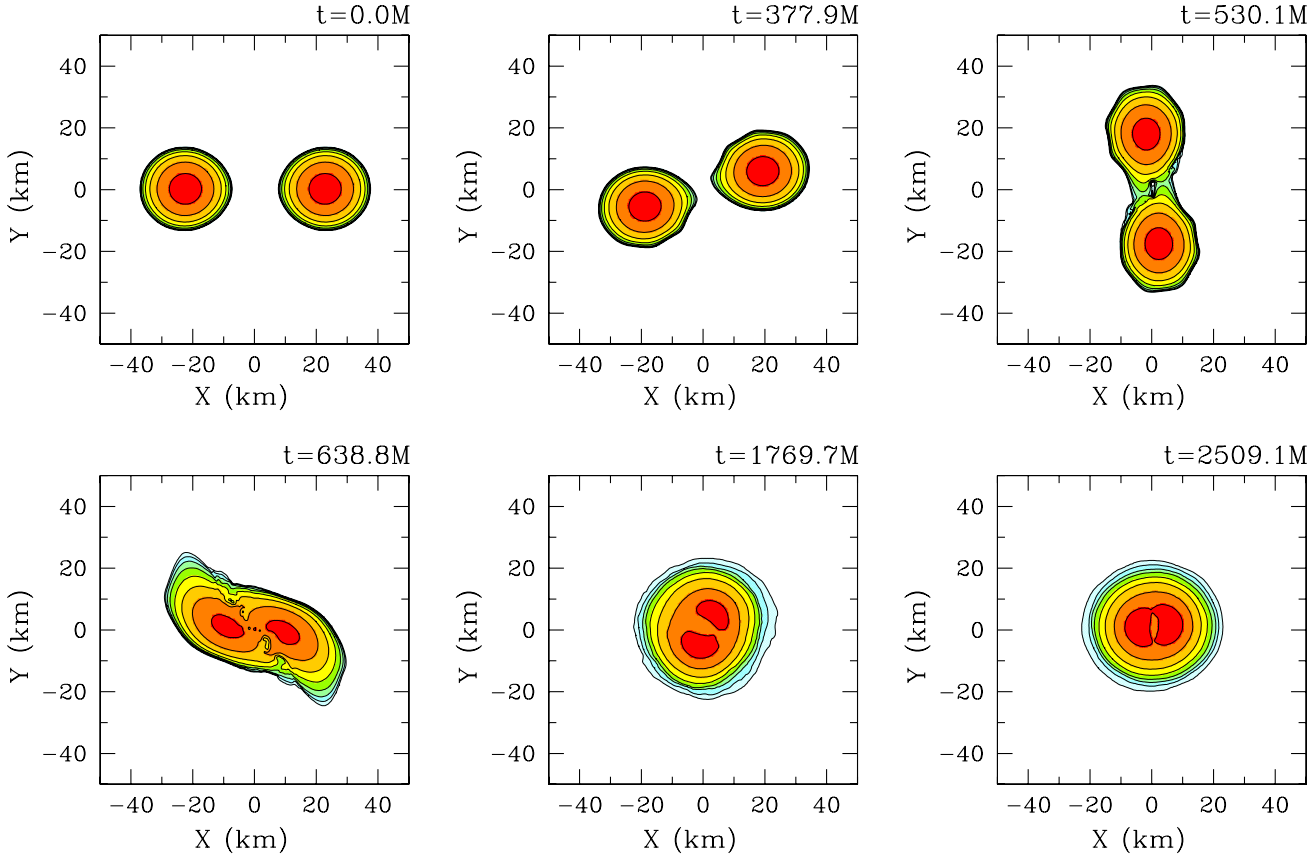

FIG. 1 (color online). Case A orbital-plane rest-mass density contours at selected times. Contours are plotted according to $\rho_0 = \rho_{0,\max}(10^{-0.375j-0.131})$, $(j = 0, 1, \ldots 8)$. The color sequence dark red, red, orange, yellow, green, light green, blue and light blue implies a sequence from higher to lower values. This roughly corresponds to darker grey-scaling for higher values. The maximum initial NS density is $\kappa\rho_{0,\max} = 0.0917$, or $\rho_{0,\max} = 4.58 \times 10^{14}$ gcm$^{-3}(1.45M_\odot/M_0)^2$. Here $M = 1.32 \times 10^{-5}(M_0/1.45M_\odot)$ s $= 3.98(M_0/1.45M_\odot)$ km is the ADM mass, and M_0 denotes the rest mass of each star.

EOS simulation (shocks allowed), additional pressure from thermal support is also present, so $t_{\rm coll}$ can be larger. In fact, in the absence of cooling, a sufficiently hot remnant may *never* collapse. This is what [27] conclude from their case M simulation, as they demonstrated that a hot TOV star could support in equilibrium a mass greater than the total mass of their merged remnant.

Given that the Γ-law EOS remnant collapses about 100 ms later than the polytropic one, it is clear that shocks play a key dynamical role. However, shocks, which occur on a hydrodynamical time scale, give rise to at least three effects:

(1) they heat the gas, increasing the total pressure support;
(2) they affect the matter profile;
(3) and they redistribute the angular momentum.

A priori it is not clear which of these effects is responsible for prolonging the HMNS lifetime, and the answer cannot be determined by comparing simulations that do not allow for shocks to those that do.

To investigate the importance of the shock-induced thermal pressure support against collapse, cooling the hot HMNS remnant is crucial. But what is the neutrino cooling time scale?

Analyzing the nascent HMNS in case A, we can now estimate a realistic cooling time scale directly from our simulation data. In Fig. 5 we show the case A orbital-plane temperature contours of the HMNS remnant. The maximum and rms temperatures are ∼22 and ∼5.5 MeV, respectively. Using these values for the neutrino energy, and setting $M = 2.7M_\odot$ and $R = 16$ km, Eq. (5) yields a neutrino diffusion time scale of ∼165 ms–2.64 s. Note that this range is consistent with our discussion in Sec. II, where the neutrino diffusion time scale was estimated to be comparable to the gravitational wave time scale of ∼120 ms.

Therefore, as the additional thermal pressure is a dynamically important source of support, then cooling must be incorporated in numerical simulations to accurately determine the time interval between merger and delayed collapse. Low energy neutrinos ($E_\nu \lesssim 10$ MeV), that escape the HMNS on a time scale $\lesssim t_{\rm GW}$, can remove a sufficiently large amount of thermal energy to accelerate the collapse. This is the main point we want to emphasize

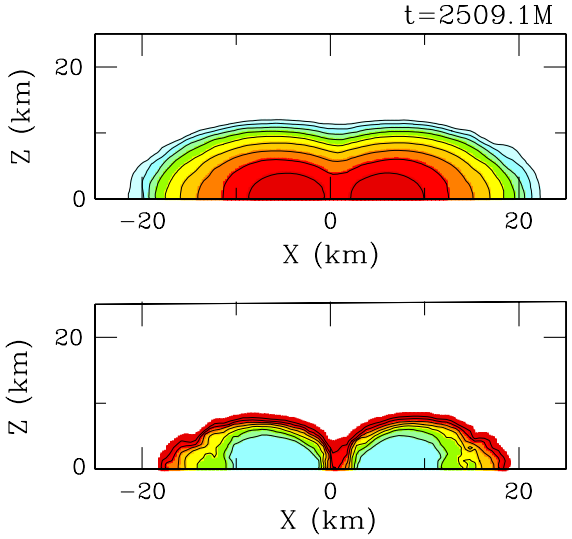

FIG. 2 (color online). Case A meridional (XZ) plane rest-mass density (upper panel) and K contours (lower panel). Density contours are plotted according to $\rho_0 = \rho_{0,\max}(10^{-0.375j-0.131})$, $(j = 0, 1, \ldots 8)$, where $\kappa\rho_{0,\max} = 0.0917$, or $\rho_{0,\max} = 4.58 \times 10^{14}$ gcm$^{-3}(1.45M_\odot/M_0)^2$. K contours are plotted according to $K = K_{\max}10^{-0.031j}$, $(j = 0, 1, \ldots 8)$. Here $K_{\max} = 1.77$. The color coding is the same as used in Fig. 1. In the lower panel light blue indicates $K \approx 1$ and dark red $K \approx 1.6$. Here $M = 1.32 \times 10^{-5}(M_0/1.45M_\odot)$ s $= 3.98(M_0/1.45M_\odot)$ km is the ADM mass, and M_0 denotes the rest mass of each star.

in this paper. Our conclusion may even be more important when a stiff EOS is employed, as the HMNS will be less compact resulting in less effective GW emission.

B. Cooling study

To assess the impact of the shock-induced thermal pressure in the HMNS remnant, we slowly remove the thermal pressure using our covariant cooling technique. We chose two cooling time scales for our study. The short one is $\tau_{c,1} = 6.5t_{\rm d}$ for case B1 and the long one is $\tau_{c,2} = 2\tau_{c,1} = 13t_{\rm d}$ for case B2, where

$$t_{\rm d} \equiv \frac{1}{\sqrt{\bar{\rho}}} \approx 23M \tag{36}$$

is the dynamical time scale of the HMNS, where $\bar{\rho}$ is the mean HMNS density. This choice is arbitrary, but it is set so that the cooling time scale is significantly longer than the dynamical time scale of the remnant, as in physically realistic stars, but short enough for our simulations to be completed within a reasonable time.

Our runs with cooling lead to BH formation within a few cooling time scales. This can be seen in the left two panels of Fig. 4 where we plot the maximum rest-mass density $\rho_{0,\max}$ and the minimum of the lapse function $\alpha_{\min}$ vs time, respectively. From these plots it becomes clear that case A does not collapse within the integration time, while both cases B1 and B2 form a BH. Notice that in cases B1 and B2, when $\rho_{0,\max}$ roughly equals two times its initial value, the lapse function collapses and a BH forms. Note that this is consistent with the polytropic runs of Ref. [25], in which shocks were suppressed. Therefore, in all cases with the adopted EOS, collapse takes place when $\rho_{0,\max} \approx 2\rho_{0,\max,\rm initial}$, when thermal energy is drained from the system.

If the collapse is driven by cooling, then we naturally expect that a longer cooling time scale will increase the lifetime of the HMNS. This is precisely what we find: the collapse in case B2 occurs later than in case B1. Further evidence of cooling-induced collapse is shown in the right panel of Fig. 4. There the tracks of $\rho_{0,\max}$ against the total angular momentum of the remnant $J_{\rm int}$ are plotted using Eq. (33). This plot demonstrates that during the post-merger evolution for the same $J_{\rm int}$, $\rho_{0,\max}$ is always larger

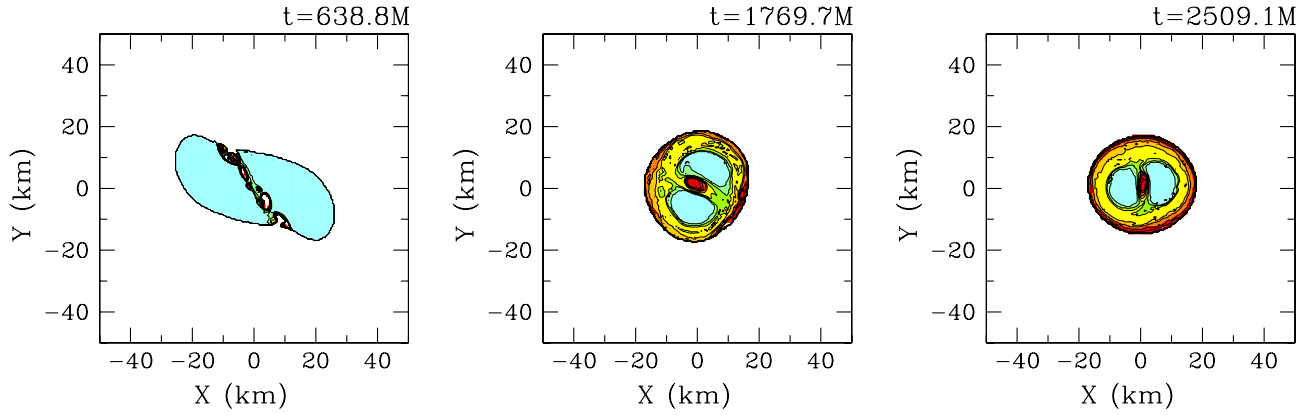

FIG. 3 (color online). Case A orbital-plane K contours at selected times. Contours are plotted according to $K = K_{\max}10^{-0.028j}$, $(j = 0, 1, \ldots 8)$. Here $K_{\max} = 1.6$. The color coding is the same as used in Figs. 1 and 2. A density cutoff of $10^{-1}\rho_{0,\max}$ has been imposed, where $\kappa\rho_{0,\max} = 0.0917$, or $\rho_{0,\max} = 4.58 \times 10^{14}$ gcm$^{-3}(1.45M_\odot/M_0)^2$. The dual cold core nature of the HMNS is visible and it becomes clear that between the two cores a hot area has formed, where 40–50% of the total pressure is due to thermal pressure. In the outer parts of the HMNS, the contribution of the thermal component is greater than 50% of the total pressure. Here $M = 1.32 \times 10^{-5}(M_0/1.45M_\odot)$ s $= 3.98(M_0/1.45M_\odot)$ km is the ADM mass, and M_0 denotes the rest mass of each star.

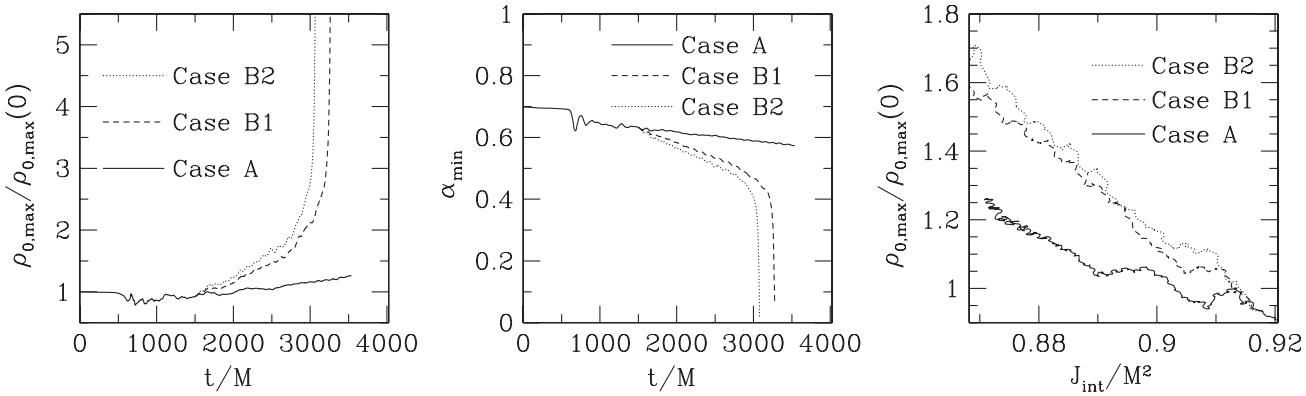

FIG. 4. Case A orbital-plane temperature contours. Contours are plotted according to $T = T_{max}10^{-0.136j}$, $(j = 0, 1, \ldots 8)$, where $T_{max} = 2.57 \times 10^{11}$ K $= 22.18$ MeV. The color coding here is the same as in Fig. 1. A density cutoff of $10^{-2}\rho_{0,max}$ has been imposed, where $\rho_{0,max}$ is the maximum density on the grid. The maximum temperature is at the center of the HMNS remnant. The rms temperature in the remnant is $\bar{T} = 6.35 \times 10^{10}$ K ≈ 5.5 MeV. Here $M = 1.32 \times 10^{-5}$ s $= 3.98$ km is the ADM mass.

with cooling present (e.g., $\rho_{0,max}$ in cases B1, B2 is $\sim$30% larger than in case A for the smallest J_{int} reached in case A). Therefore, it is the reduction of thermal pressure that leads to a more compact remnant and not angular momentum loss driven by GWs.

In Fig. 6 we show the evolution of the rest-mass density (upper row) and K contours (lower row) for case B2. The selected times correspond to 1, 8, and 11 cooling time scales after cooling was turned on [55]. The right panel corresponds to a time shortly before an apparent horizon forms. These plots indicate that as thermal pressure is removed, the double cores approach one another and the HMNS becomes more compact (notice the density increase and the shrinking size of the remnant with increasing time). We find that when the hot area between the two cores is cooled to $K \approx 1.05$, the two cores merge and form a single-core HMNS. Shortly after this occurs (at $t \approx 3000M$), the remnant undergoes catastrophic collapse.

Based on these results we conclude that thermal pressure contributes significantly to support against collapse.

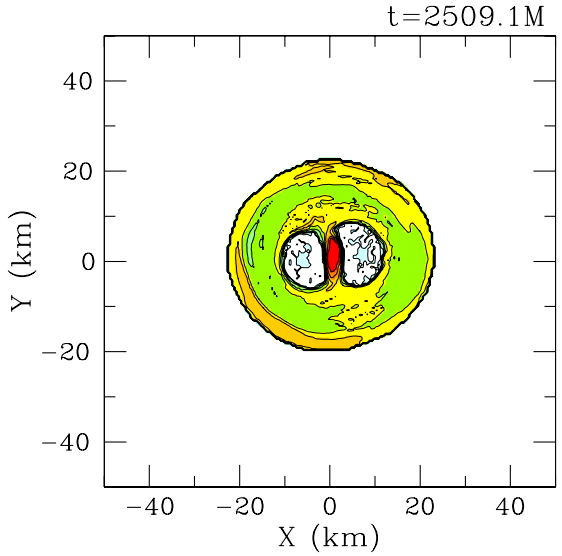

FIG. 5 (color online). Left panel: Maximum rest-mass density $\rho_{0,max}(t)$ normalized by $\rho_{0,max}(t = 0)$. Middle panel: Minimum value of the lapse function vs time. Right panel: Maximum rest-mass density vs total angular momentum for the different cooling time scales considered. Here $M = 1.32 \times 10^{-5}(M_0/1.45M_\odot)$ s $= 3.98(M_0/1.45M_\odot)$ km is the ADM mass, and $\kappa\rho_{0,max}(0) = 0.0917$, or $\rho_{0,max}(0) = 4.58 \times 10^{14}$ gcm$^{-3}(1.45M_\odot/M_0)^2$. M_0 here denotes the rest mass of each star.

C. Angular momentum conservation

Figure 7 plots the evolution of total angular momentum (J_{int}) and angular momentum carried off by GWs (ΔJ_{GW}), normalized by the ADM angular momentum of the binary (J) for cases A and B2. We find that $(J_{int} + \Delta J_{GW})/J$, which should be equal to unity at all times, is the same and close to unity for all three cases A, B1 and B2. This implies that cooling carries off negligible amounts of angular momentum which is consistent with earlier estimates [24]. The maximum violation of angular momentum conservation is $\delta J \approx 3.4\%$. Notice that J_{int} is smaller in case B2 than in case A, while ΔJ_{GW} is larger in case B2 than in case A. The distinction is due to the fact that as thermal energy is radiated away, the remnant becomes more compact, enabling GWs to remove angular momentum faster. We conclude that cooling accelerates the collapse of the HMNS by the combined action of two effects:

(1) Cooling removes thermal pressure support, yielding a more compact remnant.
(2) As the remnant becomes more compact, GWs are able to carry away angular momentum more efficiently.

VI. SUMMARY AND FUTURE WORK

A differentially rotating, quasiequilibrium HMNS is a transient configuration that can arise following the merger

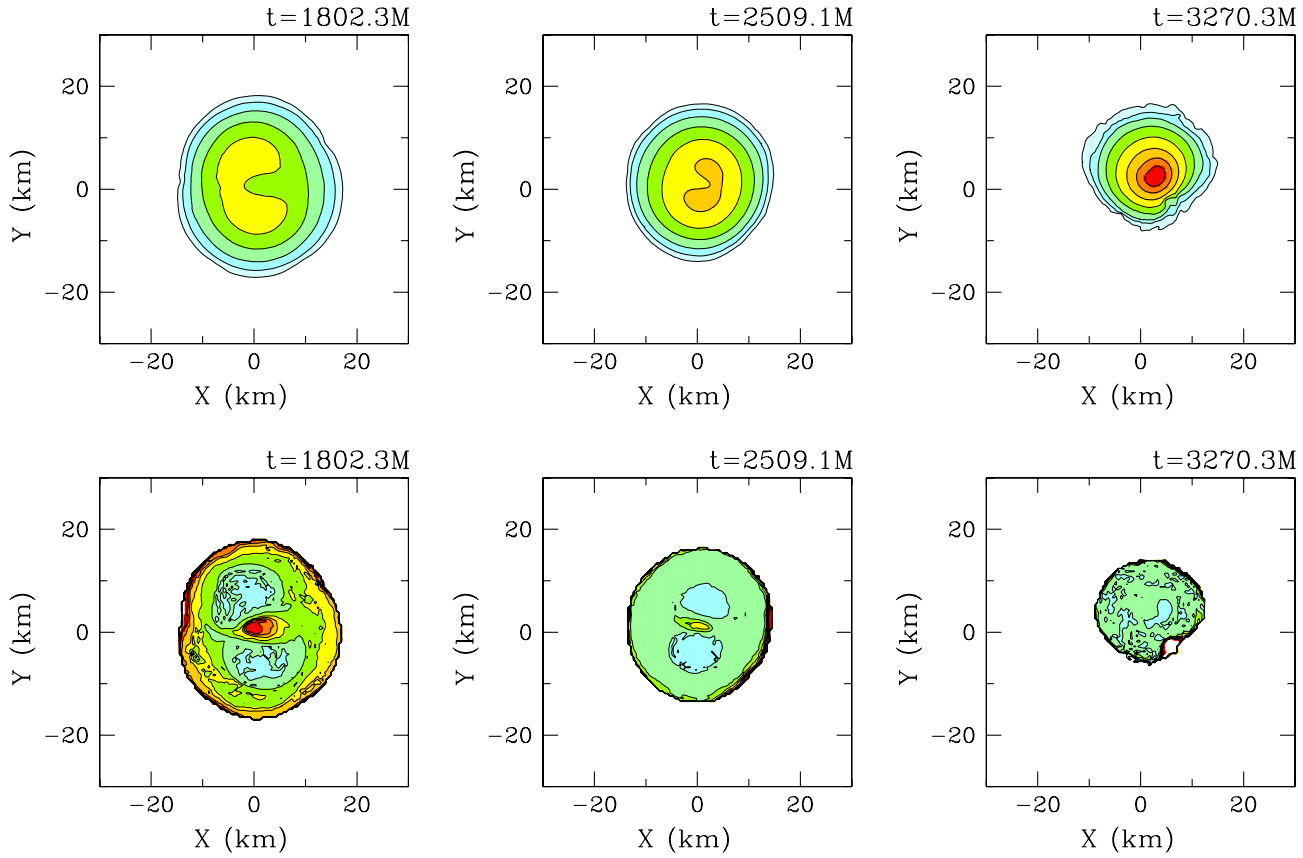

FIG. 6 (color online). Upper row: Case B2 orbital-plane rest-mass density contours at selected times. Contours are plotted according to $\rho_0 = \rho_{0,\max}(10^{-0.2j+0.568})$, $(j = 0, 1, \ldots 8)$, where $\kappa\rho_{0,\max} = 0.0917$, or $\rho_{0,\max} = 4.58 \times 10^{14}\mathrm{gcm}^{-3}(1.45M_\odot/M_0)^2$. Lower row: Case B2 orbital-plane K contours at selected times. Contours are plotted according to $K = K_{\max}10^{-0.025j}$, $(j = 0, 1, \ldots 8)$. Here $K_{\max} = 1.6$. The color coding is the same as used in Fig. 1, with light blue indicating to $K \approx 1$, yellow $K \approx 1.2$ and dark red $K \approx 1.4$. Here $M = 1.32 \times 10^{-5}(M_0/1.45M_\odot)$ s $= 3.98(M_0/1.45M_\odot)$ km is the ADM mass, and M_0 denotes the rest mass of each star.

of NSNS binaries. The mass of a HMNS is larger than the maximum mass that can be supported by a cold EOS, even with maximal uniform rotation. A HMNS will eventually undergo ''delayed collapse'' on a secular (dissipative) time scale and may power a sGRB.

When HMNSs are born in NSNS mergers, they are rapidly differentially rotating and hot due to shock heating. Therefore, HMNSs will collapse to a BH either on an angular momentum loss/magnetic braking time scale or on a cooling time scale. *A priori* it is not clear which of the two above mechanisms is most important for holding up an HMNS against collapse: centrifugal forces or thermal pressure. The answer to this question is still open and may depend on the stellar model, EOS, and initial magnetic fields.

Determining which mechanism drives a HMNS to collapse has observational consequences; the time scale of collapse will set the interval between the NSNS merger chirp signal and the delayed collapse burst signal, which may be measured by LIGO/VIRGO. Careful modeling of HMNS physics will thus place constraints on magnetic field magnitudes, the existence of bar modes, and/or the relevant cooling mechanisms. In addition, such observations could place constraints on the temperature of matter as well as the nuclear EOS.

To disentangle the effects of thermal support from those of rotational support, previous studies compared results from NSNS simulations that suppress shocks to those that allow shocks. If the HMNS remnant lives longer in the case with shocks than without, then it is tempting to infer that thermal pressure due to shock heating is solely responsible. However, it is not possible to draw such a firm conclusion because shocks, which act on a hydrodynamical time scale, not only heat the gas, thereby increasing the total pressure support, but also affect the matter profile and redistribute angular momentum. Different matter and angular momentum profiles alone can increase the lifetime of a HMNS via an increase of both the GW time scale and the amount of differential rotational support.

To address this issue, we first performed long-term, high-resolution GRHD NSNS simulations through inspiral, merger, and HMNS formation, allowing for shocks. Following HMNS formation, we continue the evolution both with and without cooling. When cooling is turned

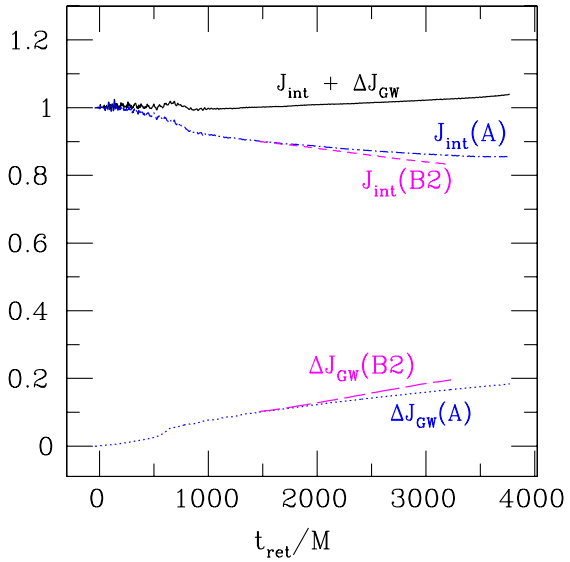

FIG. 7 (color online). Angular momentum vs time. Here $J_{\rm int}(A)$ and $\Delta J_{\rm GW}(A)$ are the total angular momentum and the angular momentum carried away by GWs, respectively, for case A. $J_{\rm int}(B2)$ and $\Delta J_{\rm GW}(B2)$ correspond to case B2. The sum in both cases is the same and given by $J_{\rm int} + \Delta J_{\rm GW}$. All quantities are normalized by the ADM angular momentum of the binary J.

off, the remnant collapses on the GW time scale. However, when cooling is turned on, we find that the HMNS collapses and forms a BH within a few cooling time scales.

Our simulations demonstrate that shock-induced thermal pressure is a significant source of support against gravitational collapse in the case of a stiff Γ-law EOS—a result consistent with simulations that employ a more realistic EOS [27]—and show explicitly that cooling can induce the catastrophic collapse of a HMNS. Estimating the temperature of the HMNS remnant, we find that a realistic neutrino cooling time scale is of order a few 100 ms. Given that the estimated cooling and angular momentum loss/magnetic braking time scales can be comparable, cooling should be accounted for to accurately determine the lifetime of a HMNS. Therefore, simulations that implement cooling will lead to earlier collapse than simulations that ignore it; otherwise, the predicted GW and electromagnetic signatures from these delayed collapse events may be incorrect.

Therefore, to accurately determine the lifetime of HMNS remnants, neutrino cooling physics should be incorporated in NSNS simulations. In the future we plan to revisit the subject using a more realistic neutrino leakage scheme, such as that used in Refs. [27,56], in conjunction with a more realistic treatment of the microphysics involved.

ACKNOWLEDGMENTS

The authors would like to thank B. Giacomazzo, Y. T. Liu, and Y. Sekiguchi for helpful discussions. This paper was supported in part by NSF Grants No. AST-1002667 and No. PHY-0963136, as well as NASA Grant No. NNX11AE11G at the University of Illinois at Urbana-Champaign.

[1] B. Abbott, and the LIGO Scientific Collaboration, Phys. Rev. D **77**, 062002 (2008).
[2] D. A. Brown, S. Babak, P. R. Brady, N. Christensen, T. Cokelaer, J. D. E. Creighton, S. Fairhurst, G. Gonzalez, E. Messaritaki, B. S. Sathyaprakash, P. Shawhan, and N. Zotov, Classical Quantum Gravity **21**, S1625 (2004).
[3] F. Acernese, and the VIRGO Collaboration, Classical Quantum Gravity **23**, S635 (2006).
[4] F. Beauville, and the LIGO-VIRGO Working Group, Classical Quantum Gravity **25**, 045001 (2008).
[5] H. Lück, and the GEO600 collaboration, Classical Quantum Gravity **23**, S71 (2006).
[6] K. Somiya, (for the LCGT Collaboration), Classical Quantum Gravity **29**, 124007 (2012).
[7] P. Amaro-Seoane, S. Aoudia, S. Babak, P. Binetruy, E. Berti *et al.*, Classical Quantum Gravity **29**, 124016 (2012).
[8] S. Kawamura, and the DECIGO collaboration, Classical Quantum Gravity **23**, S125 (2006).
[9] T. W. Baumgarte and S. L. Shapiro, *Numerical Relativity: Solving Einstein's Equations on the Computer* (Cambridge University Press, Cambridge, England, 2010).
[10] I. Hinder, Classical Quantum Gravity **27**, 114004 (2010).
[11] J. A. Faber and F. A. Rasio, Living Rev. Relativity **15**, 8 (2012).
[12] M. Shibata and K. Taniguchi, Living Rev. Relativity **14** (2011).
[13] V. Paschalidis, Z. Etienne, Y. T. Liu, and S. L. Shapiro, Phys. Rev. D **83**, 064002 (2011).
[14] V. Paschalidis, Y. T. Liu, Z. Etienne, and S. L. Shapiro, Phys. Rev. D **84**, 104032 (2011).
[15] V. Paschalidis, M. MacLeod, T. W. Baumgarte, and S. L. Shapiro, Phys. Rev. D **80**, 024006 (2009).
[16] T. W. Baumgarte, S. L. Shapiro, and M. Shibata, Astrophys. J. **528**, L29 (2000).
[17] G. B. Cook, S. L. Shapiro, and S. A. Teukolsky, Astrophys. J. **422**, 227 (1994).
[18] G. B. Cook, S. L. Shapiro, and S. A. Teukolsky, Astrophys. J. **424**, 823 (1994).
[19] M. Shibata and K. Taniguchi, Phys. Rev. D **73**, 064027 (2006).
[20] M. D. Duez, Y. T. Liu, S. L. Shapiro, and B. C. Stephens, Phys. Rev. D **69**, 104030 (2004).
[21] M. D. Duez, Y. T. Liu, S. L. Shapiro, M. Shibata, and B. C. Stephens, Phys. Rev. Lett. **96**, 031101 (2006).

[22] M. Shibata and K. Taniguchi, Phys. Rev. D **73**, 064027 (2006).

[23] Note that neutrinos, too, carry away angular momentum from the system, but according to Ref. [24], neutrino emission is very inefficient in decreasing the angular momentum of a HMNS.

[24] T. W. Baumgarte and S. L. Shapiro, Astrophys. J. **504**, 431 (1998).

[25] L. Baiotti, B. Giacomazzo, and L. Rezzolla, Phys. Rev. D **78**, 084033 (2008).

[26] L. Rezzolla, L. Baiotti, B. Giacomazzo, D. Link, and J. A. Font, Classical Quantum Gravity **27**, 114105 (2010).

[27] Y. Sekiguchi, K. Kiuchi, K. Kyutoku, and M. Shibata, Phys. Rev. Lett. **107**, 051102 (2011).

[28] S. L. Shapiro and S. A. Teukolsky, *Black Holes, White Dwarfs, and Neutron Stars* (John Wiley and Sons, New York, 1983).

[29] S. Rosswog and M. Liebendoerfer, Mon. Not. R. Astron. Soc. **342**, 673 (2003).

[30] Given the low value of $Y_e \approx 0.1$, i.e., of the mean number of electrons per baryon found in NSNS mergers in Ref. [29], in our estimates here we assume for simplicity that almost all baryons are neutrons.

[31] R. C. Duncan and C. Thompson, Astrophys. J. Lett. **392**, L9 (1992).

[32] L. Rezzolla, B. Giacomazzo, L. Baiotti, J. Granot, C. Kouveliotou, and M. A. Aloy, Astrophys. J. **732**, L6 (2011).

[33] Z. B. Etienne, J. A. Faber, Y. T. Liu, S. L. Shapiro, K. Taniguchi, and T. W. Baumgarte, Phys. Rev. D **77**, 084002 (2008).

[34] Z. B. Etienne, Y. T. Liu, S. L. Shapiro, and T. W. Baumgarte, Phys. Rev. D **79**, 044024 (2009).

[35] Z. B. Etienne, Y. T. Liu, and S. L. Shapiro, Phys. Rev. D **82**, 084031 (2010).

[36] Z. B. Etienne, V. Paschalidis, Y. T. Liu, and S. L. Shapiro, Phys. Rev. D **85**, 024013 (2012).

[37] M. Shibata and T. Nakamura, Phys. Rev. D **52**, 5428 (1995).

[38] T. W. Baumgarte and S. L. Shapiro, Phys. Rev. D **59**, 024007 (1998).

[39] J. R. van Meter, J. G. Baker, M. Koppitz, and D.-I. Choi, Phys. Rev. D **73**, 124011 (2006).

[40] http://www.lorene.obspm.fr/.

[41] http://www.cactuscode.org/.

[42] E. Schnetter, S. H. Hawley, and I. Hawke, Classical Quantum Gravity **21**, 1465 (2004).

[43] M. D. Duez, Y. T. Liu, S. L. Shapiro, and B. C. Stephens, Phys. Rev. D **72**, 024028 (2005).

[44] P. Colella and P. R. Woodward, J. Comput. Phys. **54**, 174 (1984).

[45] A. Harten, P. Lax, and B. van Leer, SIAM Rev. **25**, 35 (1983).

[46] D. Mihalas and B. W. Mihalas, *Foundations of Radiation Hydrodynamics* (Dover, New York, 1999).

[47] S. L. Shapiro, Astrophys. J. **472**, 308 (1996).

[48] B. D. Farris, T. K. Li, Y. T. Liu, and S. L. Shapiro, Phys. Rev. D **78**, 024023 (2008).

[49] S. C. Noble, C. F. Gammie, J. C. McKinney, and L. Del Zanna, Astrophys. J. **641**, 626 (2006).

[50] S. C. Noble, C. F. Gammie, J. C. McKinney, and L. Del Zanna (2006), http://rainman.astro.illinois.edu/codelib/.

[51] K. Beckwith and J. M. Stone, Astrophys. J. Suppl. Ser. **193**, 6 (2011).

[52] Z. B. Etienne, Y. T. Liu, V. Paschalidis, and S. L. Shapiro, Phys. Rev. D **85**, 064029 (2012).

[53] M. Boyle and A. H. Mroué, Phys. Rev. D **80**, 124045 (2009).

[54] M. Ruiz, M. Alcubierre, D. Núñez, and R. Takahashi, Gen. Relativ. Gravit. **40**, 1705 (2008).

[55] The corresponding plots in case B1 are similar and, therefore, not shown.

[56] Y. Sekiguchi, Classical Quantum Gravity **27**, 114107 (2010).